Dalton Transactions

ROYAL SOCIETY OF CHEMISTRY

PAPER

View Article Online
View Journal | View Issue

Cite this: *Dalton Trans.*, 2020, **49**, 2578

Structure and thermal expansion behavior of $Ca_4La_{6-x}Nd_x(SiO_4)_4(PO_4)_2O_2$ apatite for nuclear waste immobilization†

Shan Yan, Dongyan Yang, Shuangqiang Chen, Juan Wen, Wenhao He, Shiyin Ji, Yue Xia, Yinlong Wang, Liangfu Zhou and Yuhong Li*

In this study, $Ca_4La_{6-x}Nd_x(SiO_4)_4(PO_4)_2O_2$ (x = 0, 1, 2, 3, 4, 5, and 6) apatites were explored for nuclear waste immobilization, and Nd^{3+} ions were used as the surrogate of radionuclides (such as Am^{3+}, Cm^{3+}, and Pu^{3+}). The synthesized samples conform to the $P6_3/m$ (176) symmetry in the hexagonal system according to the characterizations by means of X-ray diffraction, Raman spectra, and Fourier-transform infrared spectra. Rietveld analyses indicate that both Ca^{2+} and Ln^{3+} (La, Nd) cations are located at the M_{4f} and M_{6h} sites, which is different from earlier studies. The M_{6h} sites prefer to be occupied by Ln^{3+} (La, Nd) cations with higher valence. Besides, the content of the impurity phase $Ca_3(PO_4)_2$ reduces from 2.815 wt% to 0 with the incorporation of Nd^{3+} ions. These results demonstrate that apatites possess excellent ability to accommodate radionuclides with various valences and radii at the M_{4f} and M_{6h} sites. Moreover, we investigated the thermal expansion behavior by high-temperature X-ray diffraction. There is no phase transformation in the range of 298–1173 K, and the $Ca_4La_{6-x}Nd_x(SiO_4)_4(PO_4)_2O_2$ apatites exhibit lower thermal expansion coefficients than other candidates that have been extensively studied. Furthermore, the thermal expansion coefficient gradually decreases with the accommodation of Nd^{3+} ions. All the results suggest that apatites are promising candidates for nuclear waste immobilization.

Received 30th December 2019,
Accepted 20th January 2020

DOI: 10.1039/c9dt04915k

rsc.li/dalton

1. Introduction

Today, the inventory of high-level nuclear waste, which is destined for long-term storage and eventual geologic disposal, has accumulated in large quantities.[1,2] Although borosilicate and phosphate glassy matrices have been accepted as first-generation waste forms,[2,3] there is a potential need for more appropriate and durable waste forms, such as crystalline ceramics. Therefore, many researchers have focused on various ceramic materials. In particular, these compounds containing lanthanides and actinides exist in nature for millions of years, such as pyrochlore, zircon, garnet, zirconolite, perovskite, monazite, and apatite.[2,4–9] Among them, apatites have been studied in this work due to their relatively complex structure, which is a necessity for ideal waste-form phases.[2]

In addition, earlier studies have shown that apatites exhibit high radiation resistance.[6,10] The most important factor, which has attracted the interests of researchers, is that natural apatite minerals involving significant actinides can persist in a natural nuclear reactor (Oklo) for two billion years.[11–13] Hence, many investigations on apatites have been reported for nuclear waste immobilization.[6,11,14–16] For example, Vance's and Metcalfe's groups validated that radionuclides (Pu^{3+}, Pu^{4+}, U^{4+}, and Am^{3+}) can be incorporated in the synthesized apatites.[14,15] Further, even U^{6+} can be immobilized in apatite according to John's work.[16] With regard to matrices required for immobilizing radionuclides, thermal stability is important because of the decay heat and geotherm. In earlier studies, Ravikumar and Rakovan investigated the thermal expansion behaviors of $Gd_2Zr_2O_7$ pyrochlore and $Ca_{0.8}Sr_{0.1}Pb_{0.1}La_{3.4}Ce_{0.1}Pr_{0.1}Nd_{0.1}Sm_{0.1}Gd_{0.1}Y_{0.1}(SiO_4)_3O$ apatite. Their results exhibited a larger thermal expansion coefficient,[17,18] which conflicts with the demand of ideal waste-form phases. Therefore, it is necessary to seek a crystalline phase that has a lower thermal expansion coefficient.

Most apatites with the general formula $(M_{4f})_4(M_{6h})_6(BO_4)_6Z_\delta$ belong to the $P6_3/m$ (176) space group in a hexagonal system. Here, M represents the monovalent (Li^+, Na^+, *etc.*), divalent (Ca^{2+}, Sr^{2+}, Pb^{2+}, Cd^{2+}, *etc.*), trivalent (Y^{3+}, La^{3+}, *etc.*), and tetravalent (U^{4+}, Th^{4+}, *etc.*) cations; the BO_4 group can be SiO_4^{4-},

---

School of Nuclear Science and Technology, Lanzhou University, Lanzhou, 730000, China. E-mail: liyuhong@lzu.edu.cn

† Electronic supplementary information (ESI) available: Raman spectra, local graph of powder XRD patterns, and FT-IR spectra of $Ca_4La_{6-x}Nd_x(SiO_4)_4(PO_4)_2O_2$; Rietveld fitting pattern and details of crystal structure about $Ca_4La_{6-x}Nd_x(SiO_4)_4(PO_4)_2O_2$ (x = 1, 2, 3, 4, 5, 6); SEM image of $Ca_4Nd_6(SiO_4)_4(PO_4)_2O_2$ sample prepared at 1600 °C; high-temperature powder XRD patterns, crystal data, thermal expansion coefficients, and anisotropic parameters (α_a/α_c) of $Ca_4La_3Nd_3(SiO_4)_4(PO_4)_2O_2$ (x = 0, 3, 6) apatite between 298 and 1173 K. See DOI: 10.1039/c9dt04915k

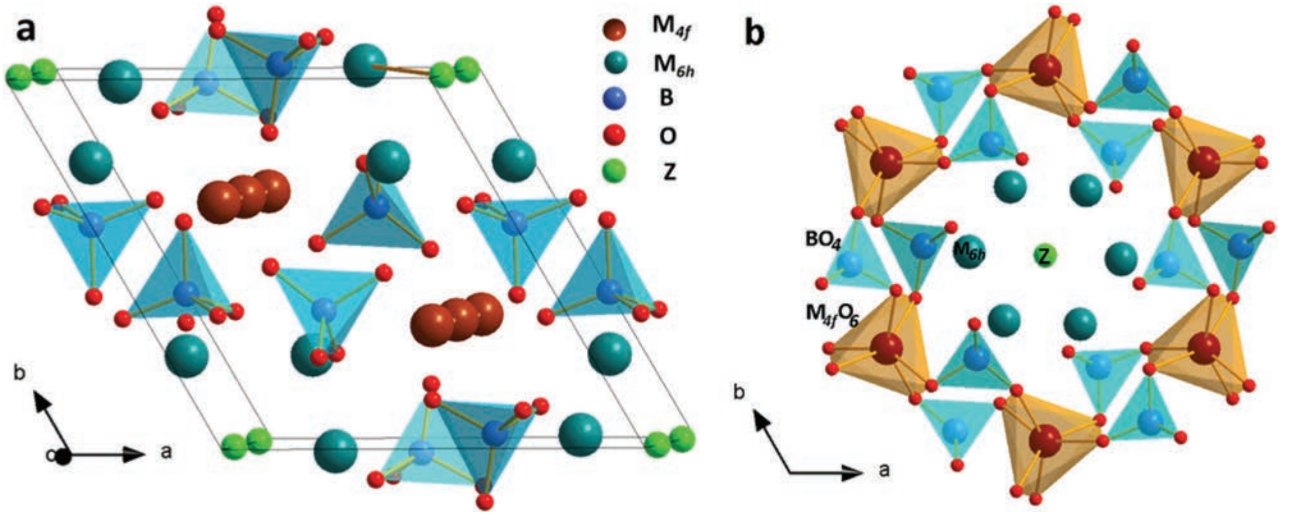

Fig. 1 (a) Schematic representation of the $(M_{4f})_4(M_{6h})_6(BO_4)_6Z_\delta$ apatite structure; (b) the $[(M_{4f})_4(BO_4)_6]$ framework encloses a one-dimensional tunnel containing the $M_{6h}Z_\delta$ component along the [001] direction.

PO_4^{3-}, VO_4^{3-}, AsO_4^{3-}, *etc.*; and Z is usually halogens, hydroxyl, or oxygen.[19–21] In the apatite structure (Fig. 1a), there are two cationic sites (M_{4f} and M_{6h}). The M_{4f} sites with the C_3 symmetry are surrounded by nine oxygen atoms, while M_{6h} sites with the C_s symmetry are coordinated with six oxygen atoms and one Z anion.[17] According to earlier studies,[21–24] the apatite structure in the $[(M_{4f})_4(BO_4)_6]$ framework (Fig. 1b), which comprise columns of face-sharing $M_{4f}O_6$ distorted trigonal prism corners connected to the BO_4 tetrahedron, enclose one-dimensional tunnels containing the $M_{6h}Z_\delta$ component along the [001] direction. Interestingly, the tunnels are appropriate to immobilize the volatile ^{129}I.[25,26] Moreover, the BO_4 groups, which may evolve into BO_3 or BO_5 units by the removal or insertion of oxygen,[19,22] can immobilize the migratory ^{99}Tc (TcO_4^-).[27,28] Indeed, the BO_4 groups are also helpful for radiation resistance. Molecular dynamics simulations on $Ca_5(PO_4)_3F$ revealed that both calcium metaprisms (Ca site) and tunnels (F site) are relatively unperturbed by forming PO_x chains even though these positions accumulate numerous defects.[29] Furthermore, the value of "δ" is flexible, such as $La_{8+x}Sr_{2-x}(SiO_4)_6O_{2+x/2}$ and $La_{10-x}Si_6O_{26+z}$,[30,31] which is very useful to maintain the charge balance considering the various decay products.

Therefore, this work was aimed to synthesize apatites with different accommodations of radionuclides and investigate the thermal expansion behavior in nuclear waste immobilization. To achieve these goals, neodymium (Nd) was used as a surrogate of radioactive actinides (such as Am^{3+}, Cm^{3+}, and Pu^{3+}) in view of the similar valences and ionic radii.[7,18,32]

2. Experimental methods

2.1 Sample preparation

The $Ca_4La_{6-x}Nd_x(SiO_4)_4(PO_4)_2O_2$ ($x = 0, 1, 2, 3, 4, 5, 6$) samples were synthesized by a conventional high-temperature solid-state method. $CaCO_3$ (99.99%), La_2O_3 (99.99%), Nd_2O_3 (99.99%), $NH_4H_2PO_4$ (99.99%), and SiO_2 (99.99%) were mixed in an appropriate stoichiometric proportion and thoroughly ground for 1 h by mechanical milling. Subsequently, these homogeneous mixtures were sintered at 1000 °C for 4 h. Then, the mixtures were pressed into pellets after being ground for another 1 h. All the pellets were sintered at 1400 °C for 18 h and allowed to naturally cool down to room temperature.

2.2 Sample characterization

All the compounds were cautiously characterized by powder X-ray diffraction (XRD) (X'Pert PRO) using Cu-Kα radiation operated at 40 mA and 40 kV at room temperature. The data were recorded from 5° to 120° at a step size of 0.02° and time per step of 1 s. The crystal structures of $Ca_4La_{6-x}Nd_x(SiO_4)_4(PO_4)_2O_2$ were determined by Rietveld refinement using the GSAS program.[33] To determine the vibrational modes, both Raman spectra (LabRAM HR 800 instrument) excited at 532 nm and Fourier-transform infrared (FT-IR) spectra (NEXUS 670 instrument) for the powders were collected at room temperature. A scanning electron microscope (SEM) with the Apreo S instrument was used to observe the morphology of the samples.

High-temperature powder XRD studies were performed using an Empyrean instrument at a heating rate of 10 °C min^{-1} from 298 to 1173 K. The data were recorded between 7° and 90° for a step size of 0.02° and a scanning rate of 4° min^{-1}. According to previous methodology,[17,34,35] we calculated the thermal expansion coefficient of the prepared samples using the unit cell parameters at different temperatures.

3. Results and discussion

3.1 Phase formation and symmetry determination

The powder XRD patterns of $Ca_4La_{6-x}Nd_x(SiO_4)_4(PO_4)_2O_2$ are shown in Fig. 2. As shown in Fig. 2a, except for the marginal peak of impurity (ICDD no.: 97-015-8736; $Ca_3(PO_4)_2$) marked with

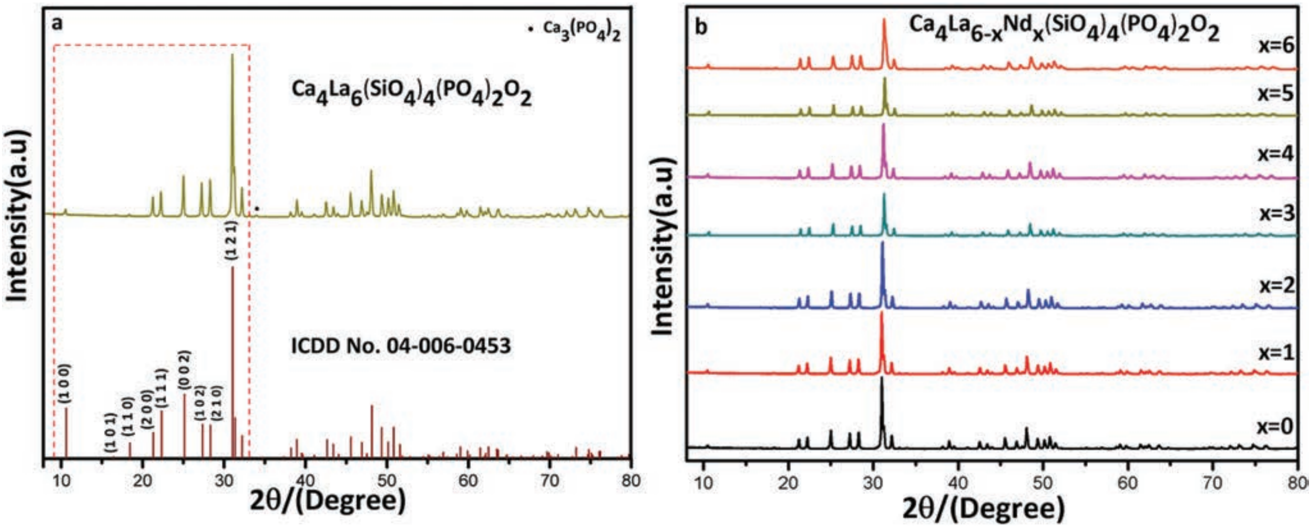

Fig. 2 (a) Powder XRD patterns of $Ca_4La_6(SiO_4)_4(PO_4)_2O_2$ as compared to the earlier model (ICDD no.: 04-006-0453; $Ca_4La_6(SiO_4)_4(PO_4)_2O_2$); (b) powder XRD patterns of $Ca_4La_{6-x}Nd_x(SiO_4)_4(PO_4)_2O_2$ (x = 0, 1, 2, 3, 4, 5, 6).

the symbol, almost all the peaks are identical as those in the earlier model (ICDD no.: 04-006-0453; $Ca_4La_6(SiO_4)_4(PO_4)_2O_2$) in the $P6_3/m$ (176) space group. There are no significant changes in the XRD patterns with an increase in the content of Nd^{3+} ions (Fig. 2b), which indicates that all the compounds conform to the apatite phase. Moreover, a slight shift in the peaks can be observed in a local graph, as shown in Fig. S1.† This phenomenon can be attributed to the smaller radius of Nd^{3+} ions than La^{3+} ions, which is consistent with Vegard's law.[36]

Nevertheless, the possibility of apatites with the $P6_3$ (173) symmetry, which has slight symmetry breaking on $m_{[001]}$ to remove the inversion symmetry of the M_{4f} site,[37,38] could not be convincingly excluded only by XRD.[37] It is still necessary to determine the correct space group symmetry when La^{3+} ions were gradually substituted by Nd^{3+} ions. Moreover, there is a need to understand whether the CO_3^{2-} groups from raw materials can be incorporated into the BO_4 sites or tunnels to form carbonized apatite, such as $Ca_9Na_{0.5}(PO_4)_{4.5}(CO_3)_{1.5}(OH)_2$ and $Ca_{10-x}(PO_4)_{6-x}(CO_3)_x(OH)_{2-x-2y}(CO_3)_y$.[39,40] Therefore, the Raman spectra and FT-IR spectra were recorded at room temperature.

According to the factor analyses of apatites in the $P6_3/m$ (176) space group,[41,42] the vibration modes could be described as follows:

$$\Gamma = 12A_g + 8E_{1g} + 13E_{2g} + 9B_g + 9A_u + 12B_{1u} + 13E_{1u} + 8E_{2u} \tag{1}$$

Only A_g, E_{1g}, and E_{2g} modes are Raman-active, while A_u and E_{1u} modes are IR-active. In the case of the $P6_3$ (173) space group, the number of modes will increase due to lower symmetry, which results in the appearance of new vibration bands in the range of the internal modes (ν_1 for symmetric stretching; ν_2 for symmetric bending; ν_3 for asymmetric stretching; and ν_4 for asymmetric bending).[37]

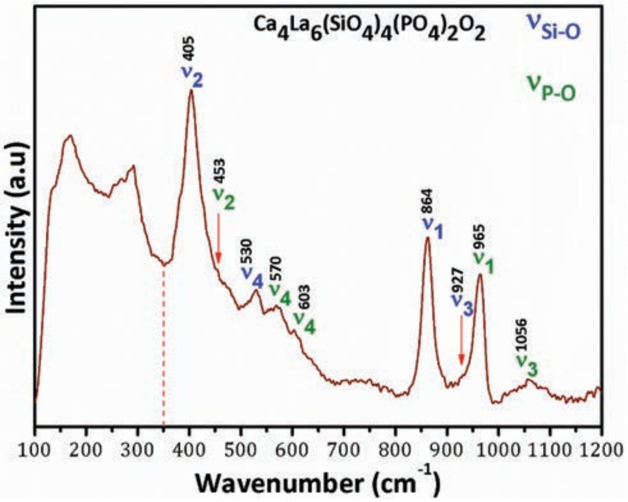

Fig. 3 Raman spectra of the $Ca_4La_6(SiO_4)_4(PO_4)_2O_2$ specimen.

The Raman spectra of the $Ca_4La_6(SiO_4)_4(PO_4)_2O_2$ apatite with the $P6_3/m$ (176) symmetry is shown in Fig. 3. Similar to the data in previous reports on the $P6_3/m$ (176) space group, the Raman spectra between 100 and 1200 cm^{-1} can be divided into two regions. The bands above 350 cm^{-1} are attributed to the internal modes of the BO_4 tetrahedron, while the bands below 350 cm^{-1} are interpreted to the complex external modes involving the translation and vibration modes of BO_4 and $M^{3+}O_n$ polyhedra.[41,43] The modes of PO_4 and SiO_4 tetrahedra are respectively marked according to earlier studies (Fig. 3).[43–46] There is an overlap between the ν_1 (PO_4) and ν_3 (SiO_4) bands, which is consistent with earlier works.[47–49] Similarly, ν_2 (PO_4) may be assigned to ~453 cm^{-1} in view of previous works and the asymmetry band from 350 to 490 cm^{-1}. The Raman spectra of other samples are shown in Fig. S2,† and the new vibration bands are not observed in the ranges of ν_1, ν_2, ν_3, and ν_4 modes. This means that the $Ca_4La_{6-x}Nd_x(SiO_4)_4(PO_4)_2O_2$ samples conform to the $P6_3/m$ (176) symmetry even though the La^{3+} ions are partly or completely substituted by Nd^{3+} ions. Moreover, the intensity of the external modes involving the vibrations of $M^{3+}O_n$ polyhedron slightly increase with the incorporation of Nd^{3+} ions possessing different polarizability toward La^{3+} ions. In addition, it should be noted that the possibility of carbonized apatite cannot be completely excluded by the Raman spectra alone because of the overlap between the ν_1 (CO_3^{2-}) and ν_3 (PO_4) bands in the range of 1000–1100 cm^{-1} for the apatite structure.[45,50]

The FT-IR spectra, which is sensitive to polar groups (such as CO_3^{2-}), is shown in Fig. 4. No features of the CO_3^{2-} groups are observed in the range of 1400–1500 cm^{-1}, which precludes the incorporation of CO_3^{2-} groups in the BO_4 sites or tunnels.[51–53] According to the published studies,[17,23,47,54–56] the characteristic bands of PO_4 detected at 1059.8 and 962.3 cm^{-1} correspond to ν_3 and ν_1 P–O stretching modes, respectively. The ν_4 and ν_2 bending modes of O–P–O separately appear at 600.5, 499.5, and 471.3 cm^{-1}. The bands at 928.8 and 868 cm^{-1} are attributed to the ν_3 and ν_1 Si–O stretching modes and the ν_2 and ν_4 bending modes are detected at 413.7 and 549.9 cm^{-1}, respectively. The transmittance at 499.5 cm^{-1} gradually decreases in the FT-IR spectra (Fig. S3†), which is difficult to exactly explain because of many factors affecting the intensity. For example, the change in dipole moment may be influenced by the distortion of the unit cell with an increase in the concentration of Nd^{3+} ions. Moreover, this phenomenon may be ascribed to the slight content of the impurity phase ($Ca_3(PO_4)_2$) detected in the similar vibration band at around 497 cm^{-1}.[57] In addition, the bands considerably shift to higher wavenumbers (Table 1), which means that more energy is needed for the vibration of SiO_4/PO_4 groups. This shift may be caused by the inductive effect or the change of bond length (SiO_4/PO_4) due to the different radii of La^{3+} and Nd^{3+} ions.

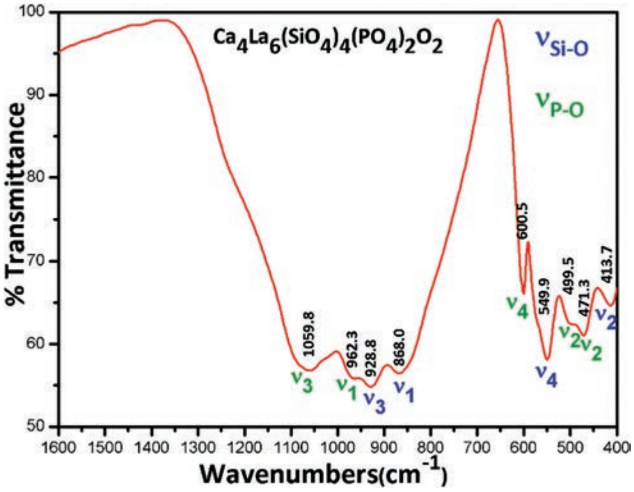

Fig. 4 FT-IR spectra of the $Ca_4La_6(SiO_4)_4(PO_4)_2O_2$ sample.

As discussed above, the XRD patterns are identical with the earlier model of the $P6_3/m$ (176) space group (Fig. 2b). Furthermore, new vibration bands owing to lower symmetry are not observed in the Raman and FT-IR spectra in the range of internal modes. These results demonstrate that the synthesized $Ca_4La_{6-x}Nd_x(SiO_4)(PO_4)_2O_2$ (x = 0, 1, 2, 3, 4, 5, 6) samples are also consistent with the $P6_3/m$ (176) symmetry.

3.2 Crystal structure analysis

The powder XRD patterns of $Ca_4La_{6-x}Nd_x(SiO_4)(PO_4)_2O_2$ exhibit slight differences in the relative intensities when compared with those of the earlier model (Fig. 2a and b), such as the (1 0 0), (1 1 0), (0 0 2), (1 0 2), and (1 2 1) lattice planes. Considering the X-ray diffraction theory as well as the literature on apatite structures,[19,20,58] the difference in intensities can be attributed to the mixed arrangements of Ca^{2+} and Ln^{3+} (Ln = La, Nd) ions between the M_{4f} and M_{6h} sites. For X-ray diffraction, the structure factor, $|F(hkl)|^2$, involving the structural information of the crystal could be expressed as follows:[58]

$$|F(hkl)|^2 = \left\{ \sum_{j=1}^{n} g^j t^j(s) f^j(s) \exp\left[2\pi i(\mathrm{h} \cdot x^j + k \cdot y^j + l \cdot z^j)\right] \right\}^2 \tag{2}$$

where n represents the number of atoms in the unit cell; $S = \sin\theta(hkl)/\lambda$; t^j is the temperature factor; and f^j and g^j refer to the atomic scattering factor and occupation factor of the j atom, respectively. Moreover, the diffraction intensity was proportional to the structure factor. It is obvious that the intensity can be affected by the occupation factor. To clearly understand this, the diffraction patterns with different occupations at the

Table 1 Assignment of the FT-IR vibration bands (cm^{-1}) for the $Ca_4La_{6-x}Nd_x(SiO_4)_4(PO_4)_2O_2$ samples; "*" denotes the indistinguishable position due to overlapping

	PO_4^{3-}					SiO_4^{4-}			
X	ν_1	ν_2		ν_3	ν_4	ν_1	ν_2	ν_3	ν_4
0	962.3	471.3	499.5	1059.8	600.5	868.0	413.7	928.8	549.9
1	964.3	474.7	501.4	1060.7	601.1	869.4	413.3	930.2	550.8
2	965.2	478.1	*	1060.9	601.5	868.7	414.9	930.8	551.4
3	966.5	481.1	*	1061.5	602.3	867.9	415.5	931.3	552.1
4	968.0	482.8	*	1061.5	602.4	868.0	417.3	933.7	553.2
5	968.8	483.9	*	1062.5	603.0	872.2	418.6	934.6	553.6
6	970.1	476.2	505.4	1060.7	603.3	880.0	419.3	934.0	555.2

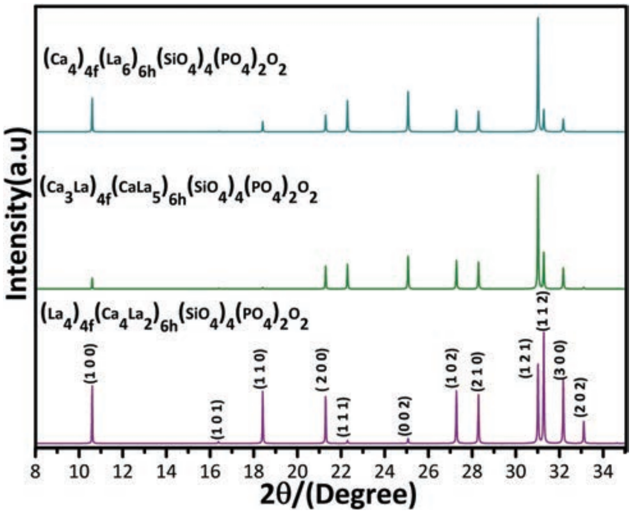

Fig. 5 XRD patterns of $Ca_4La_6(SiO_4)_4(PO_4)_2O_2$ with different occupations between the M_{4f} and M_{6h} sites simulated using the Vesta software, and other parameters (coordination, lattice parameter) were cited from the earlier model (ICDD no.: 04-006-0453; $Ca_4La_6(SiO_4)_4(PO_4)_2O_2$).

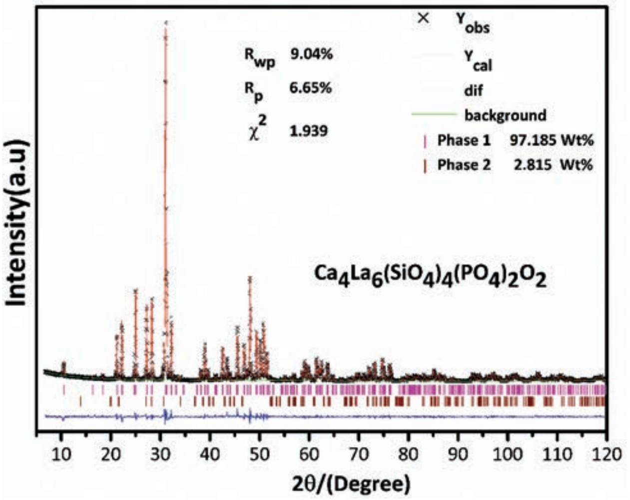

Fig. 6 Rietveld fitting pattern for the $Ca_4La_6(SiO_4)_4(PO_4)_2O_2$ sample; lines and dots denote the observed and calculated profile intensities, respectively. Short vertical bars represent the Bragg reflection positions. The difference (observed − calculated) is plotted below.

two sites were simulated by the Vesta software (Fig. 5).[59] The discrepancy in intensities can be remarkably observed with different occupations at the two sites. As studied in the earlier model (ICDD no.: 04-006-0453; $Ca_4La_6(SiO_4)_4(PO_4)_2O_2$), the Ca^{2+} and La^{3+} ions are located at the M_{4f} and M_{6h} sites, respectively. However, the possibility that both divalent and trivalent cations are located at the M_{4f} and M_{6h} sites was also reported.[19–21]

To determine the detailed crystal structure involving the distributions of Ca^{2+} and Ln^{3+} (Ln = La, Nd) ions between the M_{4f} and M_{6h} sites, Rietveld refinement was performed by using the GSAS program with a pseudo-Voigt /FCJ Asym peak shape profile in the $P6_3/m$ (176) space group. For each data series, unit cell parameters, zero error, background, and peak profile were refined, where the temperature displacement parameters and occupation factors were maintained constant (Ca^{2+} and Ln^{3+} ions were located at the M_{4f} and M_{6h} sites, respectively). After several cycles, the occupations of Ca^{2+} and Ln^{3+} were allowed to vary between the M_{4f} and M_{6h} sites. Here, the occupation factors of the M_{4f} and M_{6h} sites were independently constrained to 1. Moreover, the multipliers of occupancy on the M_{4f} and M_{6h} sites were set to 2 and 3, respectively, for the conservation of mass. Subsequently, the positions for all the atoms were refined. Finally, the isotropic temperature displacement parameters were released during the refinement process. Excellent matching to the data ($Ca_4La_6(SiO_4)_4(PO_4)_2O_2$) was obtained, as shown in Fig. 6, and the data for the other samples are shown in Fig. S4–S9.† Details regarding the crystal structure such as the atomic positions, occupations, temperature displacement parameters, selected bond lengths, and bond valence sums (BVS) are provided in Tables S1 and S2.† The small discrepancy between the ideal valence state (Ca^{2+}, La^{3+}, Nd^{3+}) and the calculated BVS values was acceptable. The discrepancy gradually decreased with an increase in the content of Nd^{3+} ions, which demonstrated that a change in bond length is reasonable during the refinement process. The Ca^{2+} cations of around 75% were found to reside at the M_{4f} sites, which is similar to those observed in earlier works where the cations with lower valence were unfavorable to occupy the M_{6h} sites.[60–62] Moreover, theoretical works have shown that the free energy of system is considerably lower if the Ln^{3+} (Ln = La, Nd) and Cs^+ cations are located at the M_{6h} and M_{4f} sites, respectively.[63–65] This is because O_4, called "free oxygen", does not belong to any BO_4 tetrahedron, and the sum of the electrostatic bond strengths of the cations toward O_4 is considerably less than 2 as required by Pauling's electrostatic valence rule even in the case of trivalent lanthanide ions.[66] Hence, the M_{6h} sites are preferred by cations with higher valences. In this work, the Ln^{3+} (La and Nd) and Ca^{2+} cations tend to occupy the M_{6h} and M_{4f} sites, respectively.

Fig. 7a shows the refined cell parameters and the decreased tendency conform to the slight shift in the diffraction peaks (Fig. S1†). Moreover, the average Si/P–O bond distance tends to slightly decrease with an increase in the content of Nd^{3+} ions (Fig. 7b), which conforms to the shifted bands of the FT-IR spectra (Table 1). The change in the energy of the IR-active vibrations is consistent with the "harmonic oscillator model".[23] That is, the bands would shift to higher wavenumbers with an increase in the bond strengths (or decrease in the bond distances). However, the decreasing average Si/P–O bond lengths (Table S2†) were close to the average value of 1.5933 Å as calculated from the Si–O (1.61 Å) and P–O (1.56 Å) values, which also demonstrate that the refinement results are reasonable. Furthermore, the inductive effect has an impact on the energy of IR-active vibrations. The electron densities of O ions connected to the Ca/La/Nd (at the M_{6h} site) and Si/P atoms are influenced by the higher bond strengths to M_{6h} sites, which

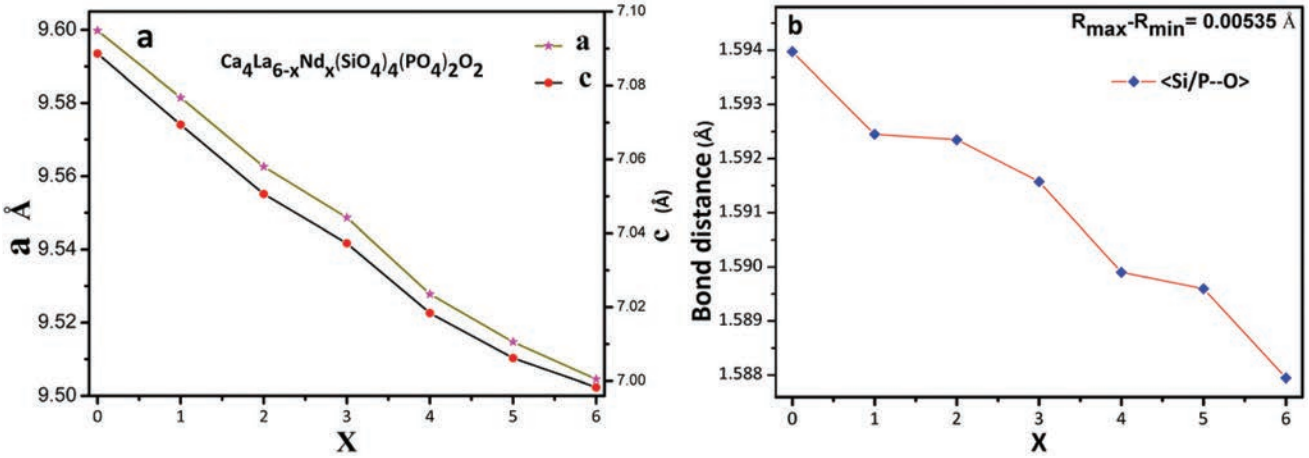

Fig. 7 Variations in cell parameters (a) *a* and *c* and (b) unit cell volume with the degree of Nd substitution *x* in the $Ca_4La_{6-x}Nd_x(SiO_4)_4(PO_4)_2O_2$ (x = 0, 1, 2, 3, 4, 5, 6) samples; the average bond distances of <Si/P–O> and <M_{6h}–O> are shown in (c) and (d), respectively.

increase the wavenumber due to a higher inductive effect. The average bond distances of <M_{6h}–O> gradually decrease (Table S2†), and the enhanced bond strength would increase the energy of IR-active vibrations, too. Therefore, the shifting of the bands to higher wavenumbers is the result of this inductive effect as well as the decreased average Si/P–O distance. Interestingly, Rietveld analysis shows that the content of $Ca_3(PO_4)_2$ impurity reduces from 2.815 wt% to 0 as the concentration of Nd^{3+} ions (used as a surrogate of radioactive actinides) increases (Fig. 8). This result shows that the $Ca_4La_{6-x}Nd_x(SiO_4)_4(PO_4)_2O_2$ apatites possess an excellent ability to accommodate radionuclides.

3.3 Morphology and crystal grain analysis

The SEM image of the $Ca_4La_6(SiO_4)_4(PO_4)_2O_2$ ceramic sample is shown in Fig. 9. The crystalline grains are rod-like, which is consistent with earlier reports on apatites.[11,67] Moreover, crystalline grains obviously contract with the accommodation of Nd^{3+} ions (Fig. 10). With regard to the $Ca_4Nd_6(SiO_4)_4(PO_4)_2O_2$ ceramic sample, it seems to only crystallize and not grow to rod-like crystalline grains under such preparation conditions. Generally, the grain growth can be expressed by the following empirical equation:[68,69]

$$G^n - G_0{}^n = t \times k_0 \exp\left(\frac{-Q}{K_B \times T}\right) \qquad (3)$$

where G and G_0 represent the average grain sizes before and after annealing, respectively; T and t refer to the temperature and time, respectively; K_B is the Boltzmann constant; n is a mechanism-dependent parameter; and Q is the activation energy that governs grain growth. In this work, the smaller crystalline grains indicate that the $Ca_4Nd_6(SiO_4)_4(PO_4)_2O_2$ sample needs higher activation energy. That is, the crystalline grain of $Ca_4Nd_6(SiO_4)_4(PO_4)_2O_2$ will grow into a rod-like shape at higher temperatures. The SEM image of the $Ca_4Nd_6(SiO_4)_4(PO_4)_2O_2$ sample at 1600 °C also proves this

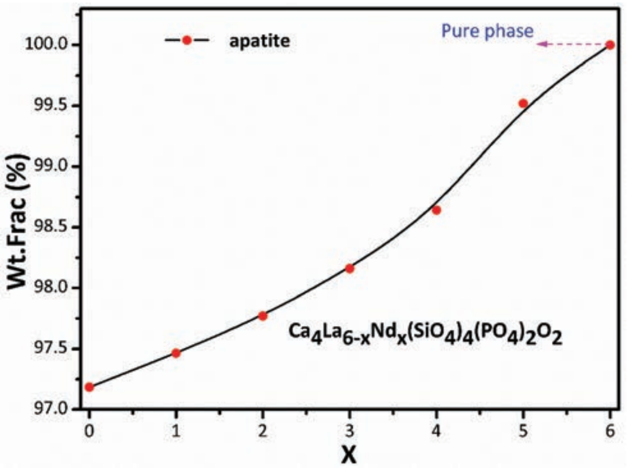

Fig. 8 Contents of apatite phase in sensitized samples with the degree of Nd substitution *x* in the $Ca_4La_{6-x}Nd_x(SiO_4)_4(PO_4)_2O_2$ (x = 0, 1, 2, 3, 4, 5, 6) samples.

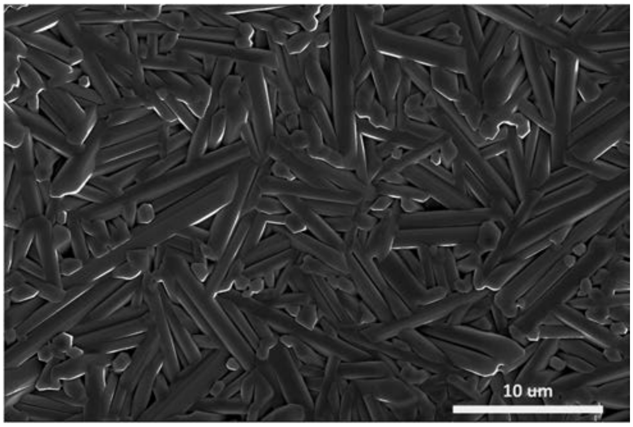

Fig. 9 SEM images of the $Ca_4La_6(SiO_4)_4(PO_4)_2O_2$ ceramic samples.

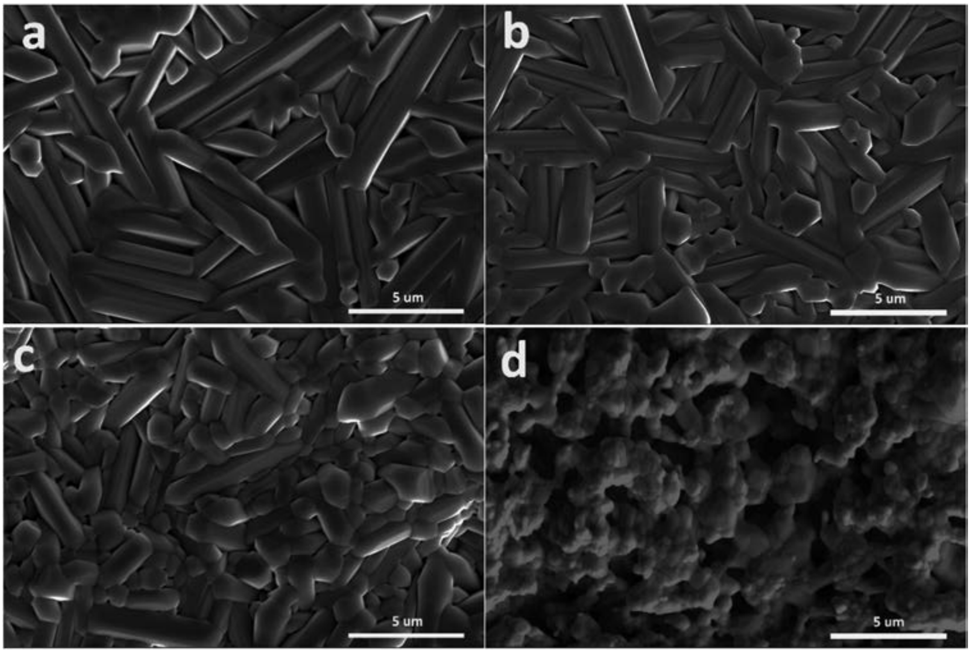

Fig. 10 SEM images of the $Ca_4La_{6-x}Nd_x(SiO_4)_4(PO_4)_2O_2$ ceramic samples for (a) $x = 0$, (b) $x = 2$, (c) $x = 4$, and (d) $x = 6$.

(Fig. S10†). Therefore, the incorporation of Nd may enhance the melting point.

Furthermore, the tendency of contracting grains is also indicated in the XRD patterns of the ceramic samples as compared to powders (Fig. 2b and 11). For the $Ca_4La_6(SiO_4)_4(PO_4)_2O_2$ specimen, the related intensities of the peaks, such as the (2 0 0), (2 1 0), (3 0 0), and (1 3 0) lattice planes, are considerably different for detecting in ceramics and powders. This phenomenon can be ascribed to the preferred orientation of the XRD patterns rather than the different structural factors as mentioned above. Generally, the theory of powder diffraction is based on completely random distributions of the orientations of the crystallites such that every lattice plane has the same probability for diffraction.[58] In practice, the external shape of the crystallites plays an important role in achieving randomness of their orientations. The anisotropic shapes, such as rod-like, needle-like, and platelet-like, give rise to distinctly nonrandom crystallite orientations, which cause distortions in intensities.[58] In this work, the distortions in intensities between ceramic and powder gradually weaken, since the smaller grains (rod-shaped shortening) can positively affect the achievement of randomness in their orientations.

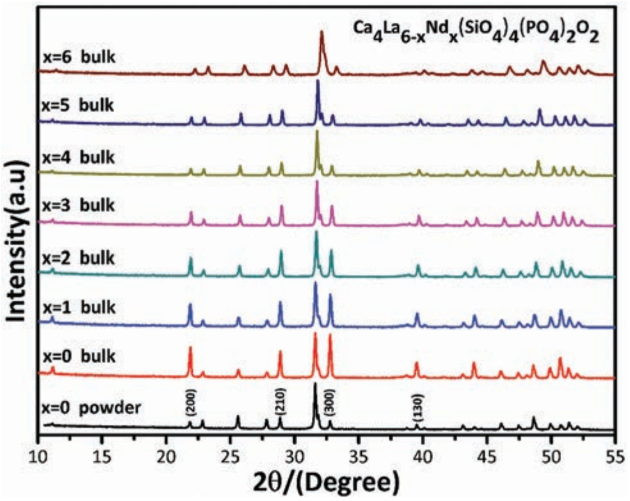

Fig. 11 Comparison of the XRD patterns of the $Ca_4La_{6-x}Nd_x(SiO_4)_4(PO_4)_2O_2$ (x = 0, 1, 2, 3, 4, 5, 6) ceramic samples.

4. Thermal expansion behavior

The thermal expansion behavior of $Ca_4La_{6-x}Nd_x(SiO_4)_4(PO_4)_2O_2$ (x = 0, 3, 6) compounds were studied using high-temperature powder XRD from 298 to 1173 K, as shown in Fig. S11–S13.† Notably, a new phase was not observed in this temperature range, which reveals that the $Ca_4La_{6-x}Nd_x(SiO_4)_4(PO_4)_2O_2$ apatites possess good thermal stability. The lattice parameters, which gradually increase with the temperature (Fig. 12), are well fitted using the following second-order polynomial:

For the $x = 0$ specimen,

$$a(T) = 9.56899 + (9.56484 \times 10^{-5})T - (1.53004 \times 10^{-8})T^2$$

$R^2 = 0.99985$

$$c(T) = 7.07086 + (5.42648 \times 10^{-5})T - (7.93347 \times 10^{-9})T^2$$

$R^2 = 0.99926$

For the $x = 3$ specimen,

$$a(T) = 9.51532 + (8.68899 \times 10^{-5})T - (1.1098 \times 10^{-8})T^2$$

$R^2 = 0.99975$

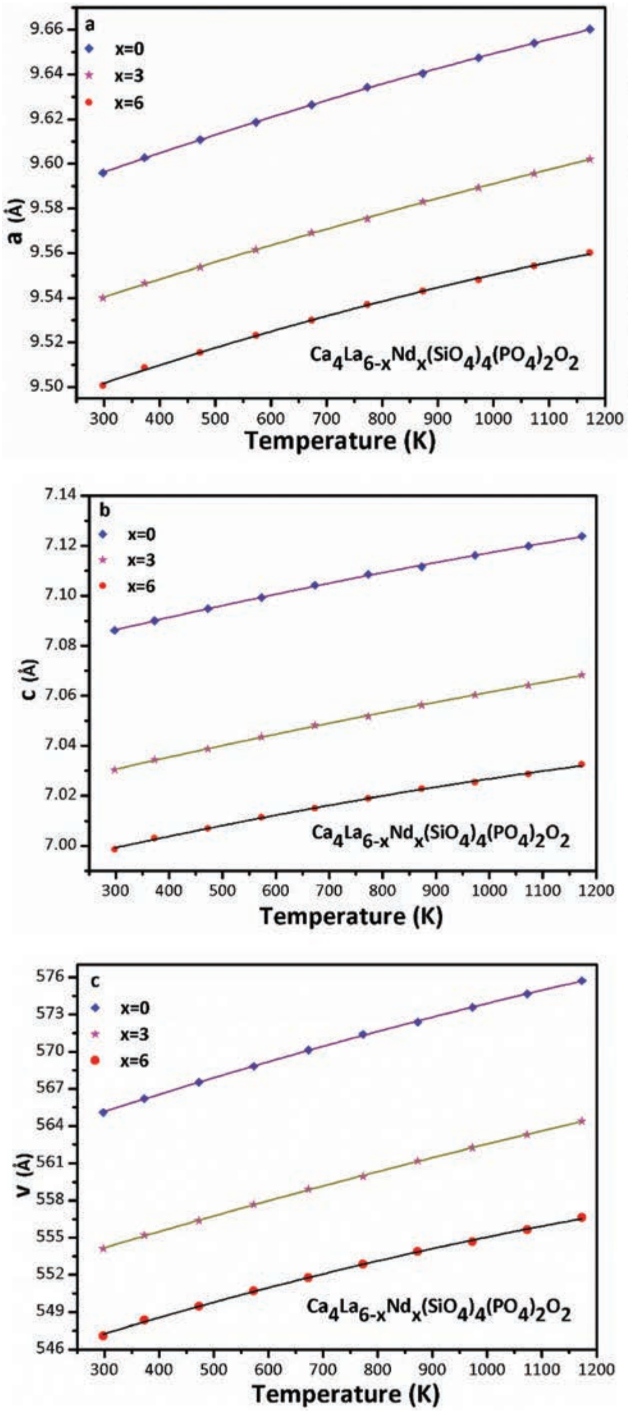

Fig. 12 Variations in the cell parameters as a function of temperature in the range of 298–1173 K for the (a) $Ca_4La_6(SiO_4)_4(PO_4)_2O_2$, (b) $Ca_4La_3Nd_3(SiO_4)_4(PO_4)_2O_2$, and (c) $Ca_4Nd_6(SiO_4)_4(PO_4)_2O_2$ specimens.

$c(T) = 7.01552 + (5.23168 \times 10^{-5})T - (6.36549 \times 10^{-9})T^2$ $R^2 = 0.99963$

For the $x = 6$ specimen,

$a(T) = 9.47509 + (9.46563 \times 10^{-5})T - (1.9291 \times 10^{-8})T^2$ $R^2 = 0.99893$

$c(T) = 6.98436 + (5.28433 \times 10^{-5})T - (1.04365 \times 10^{-8})T^2$ $R^2 = 0.99837$

As studied before,[34,70] the line thermal expansion coefficient (α) and average line thermal expansion coefficient (α') are defined by the following equations, respectively:

$$\alpha(T) = \frac{1}{A_0} \times \frac{\mathrm{d}A}{\mathrm{d}T} \tag{4}$$

$$\alpha' = \frac{1}{A_0} \times \frac{(A - A_0)}{(T - T_0)} \tag{5}$$

where A_0 and A represent the values of cell paraments at 298 K (T_0) and other temperatures (T). For the three compounds, the calculated line thermal expansion coefficients (α_a and α_c) dependent on temperature are shown in Fig. 13. Moreover, the volume thermal expansion coefficients and anisotropic parameters (α_a/α_c) are provided in Tables S3–S5.† The thermal expansion coefficients of $Ca_4La_{6-x}Nd_x(SiO_4)_4(PO_4)_2O_2$ compounds gradually decrease with an increase in temperature, which is different than that observed in most materials.[17,24,35,71–73] However, a few studies on the apatite structure have also given similar results.[74–76] This phenomenon indicates that the degree of thermal expansion becomes weak in the same temperature range, which may result from the stable and complex structure constraining the cells to sustainable growth.

Moreover, the calculated average thermal expansion coefficients as a function of composition are shown in Fig. 14. Evidently, α'_a, α'_c, and α'_v tend to decrease with an increase in the concentration of Nd^{3+} ions. In general, materials with lower average thermal expansion coefficients possess a higher melting point according to the empirical relationship.[77,78] This relationship confirms our assumption from the SEM results. To clearly understand the thermal expansion behavior, the lattice energy, which is an inverse of the thermal expansion coefficient of the material,[79,80] should also be taken into account. In fact, the lattice energy gradually increased with a decrease in the cell volume.[81] Therefore, the decreased thermal expansion coefficient can be attributed to the enhanced lattice energy. In the comparative analysis of the thermal expansion behavior to the other candidates, particularly for the extensively studied pyrochlores, $Gd_{2-x}Nd_xZr_2O_7$ ($\alpha'_a = 11.91 \rightarrow 11.16 \times 10^{-6}\ K^{-1}$),[18] $Gd_2Ce_xZr_{2-x}O_7$ ($\alpha'_a = 11.6 \rightarrow 13.8 \times 10^{-6}\ K^{-1}$),[82] and $(RE_{0.9}Sc_{0.1})_2Zr_2O_7$ (RE = La, Sm, Dy, Er) ($\alpha'_a > 9.8 \times 10^{-6}\ K^{-1}$),[83] the $Ca_4La_{6-x}Nd_x(SiO_4)_4(PO_4)_2O_2$ apatites exhibit lower expansion coefficients ($\alpha'_a = 7.66 \rightarrow 7.16 \times 10^{-6}\ K^{-1}$; $\alpha'_c = 6.06 \rightarrow 5.53 \times 10^{-6}\ K^{-1}$). Therefore, this apatite with a lower thermal expansion coefficient may be a better candidate for immobilizing high-level waste.

5. Conclusion

In summary, $Ca_4La_{6-x}Nd_x(SiO_4)_4(PO_4)_2O_2$ (x = 0, 1, 2, 3, 4, 5, 6) apatites were synthesized by a high-temperature solid-state method and characterized by XRD, FT-IR, Raman, and SEM. All the compounds possess the apatite structure in the $P6_3/m$ (176) space group. Different to earlier studies, Rietveld analyses

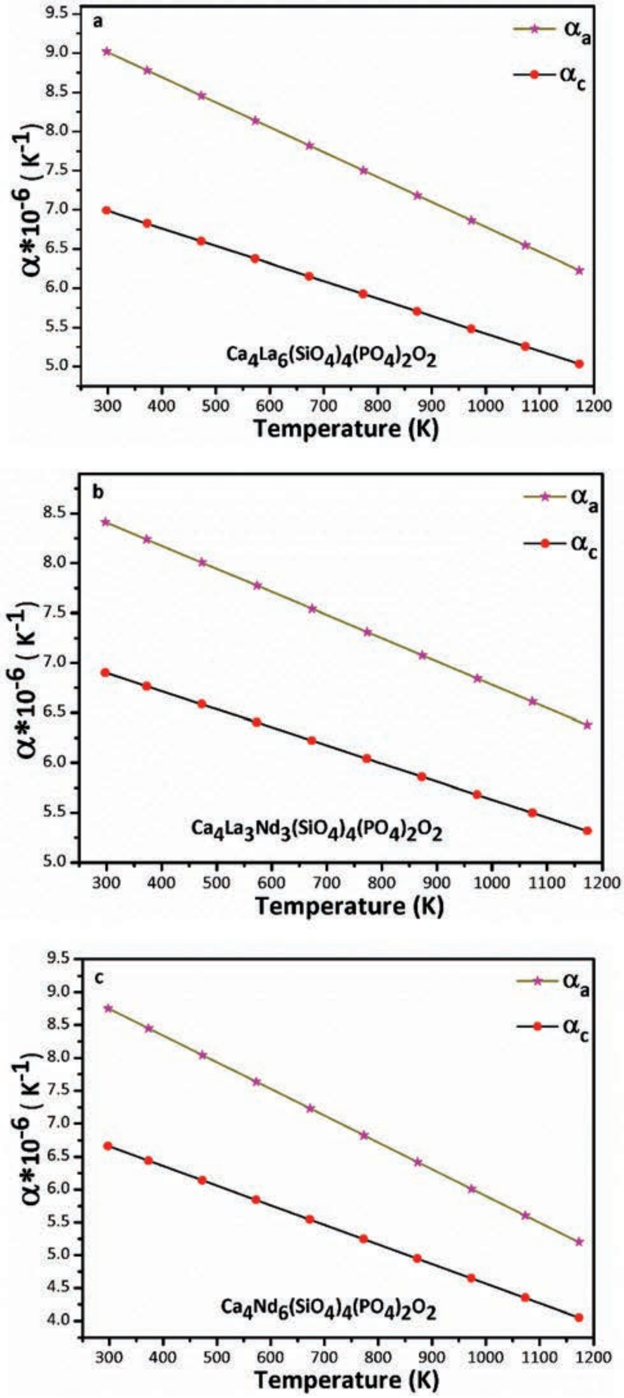

Fig. 13 Variations in the thermal expansion coefficients as a function of temperature in the range of 298–1173 K for the (a) $Ca_4La_6(SiO_4)_4(PO_4)_2O_2$, (b) $Ca_4La_3Nd_3(SiO_4)_4(PO_4)_2O_2$, and (c) $Ca_4Nd_6(SiO_4)_4(PO_4)_2O_2$ specimens.

demonstrated that both Ca^{2+} and Ln^{3+} (La, Nd) cations were located at the M_{4f} and M_{6h} positions. Moreover, the M_{6h} site preferred to be occupied by Ln^{3+} (La, Nd) cations with higher valences. This result indicates that both M_{4f} and M_{6h} sites of the apatite can be used to immobilize radionuclides. Similarly, the decreased content of the impurity phase ($Ca_3(PO_4)_2$; from 2.815 wt% to 0) and the enhanced melting point suggest that the apatite system possesses higher chemical stability due to the incorporation of Nd^{3+} ions (a surrogate of Am^{3+}, Cm^{3+}, and Pu^{3+}). In addition, these $Ca_4La_{6-x}Nd_x(SiO_4)_4(PO_4)_2O_2$ compounds exhibit lower thermal expansion coefficients as compared to most candidates used for nuclear waste immobilization.[17,18,24,82,83] Furthermore, the thermal expansion coefficient of the apatite gradually decreases with the accommodation of Nd^{3+} ions, which is induced by the enhanced lattice energy. All these results imply that apatites with better thermal and chemical stabilities are promising candidates for nuclear waste immobilization.

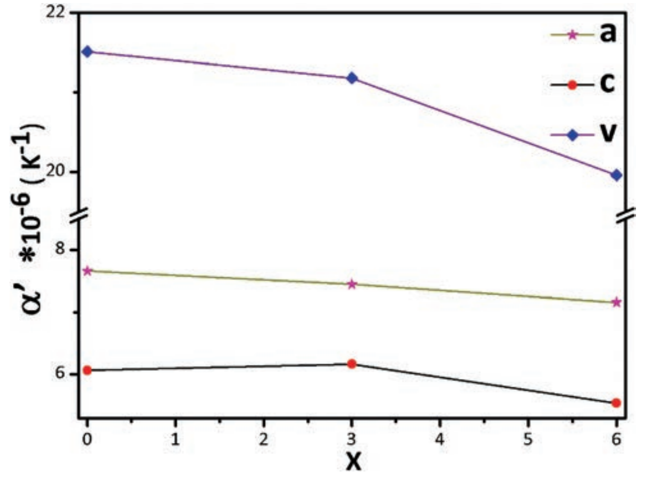

Fig. 14 Changes in the average expansion coefficient (α'_a, α'_c, and α'_v) with the composition in the $Ca_4La_{6-x}Nd_x(SiO_4)_4(PO_4)_2O_2$ series.

Conflicts of interest

There are no conflicts to declare.

Acknowledgements

The reported study was supported by project supported by the National Natural Science Foundation of China (Grant No. 11775102 and 11805088), the Open Project of State Key Laboratory of Environment-friendly Energy Materials (No. 18kfhg05), and the Fundamental Research Funds for the Central Universities (Lanzhou University, No. lzujbky-2018-19).

References

1 R. C. Ewing, *Nat. Mater.*, 2015, **14**, 252–257.
2 W. J. Weber, R. C. Ewing, C. R. A. Catlow, T. D. de la Rubia, L. W. Hobbs, C. Kinoshita, H.J. Matzke, A. T. Motta, M. Nastasi, E. K. H. Salje, E. R. Vance and S. J. Zinkle, *J. Mater. Res.*, 1998, **13**, 1434–1484.

3 I. W. Donald, B. L. Metcalfe and R. N. J. Taylor, *J. Mater. Sci.*, 1997, **32**, 5851–5887.

4 S. Park, M. Lang, C. L. Tracy, J. Zhang, F. Zhang, C. Trautmann, M. D. Rodriguez, P. Kluth and R. C. Ewing, *Acta Mater.*, 2015, **93**, 1–11.

5 Y. H. Li, B. P. Uberuaga, C. Jiang, S. Choudhury, J. A. Valdez, M. K. Patel, J. Won, Y. Q. Wang, M. Tang, D. J. Safarik, D. D. Byler, K. J. Mcclellan, I. O. Usov, T. Hartmann, G. Baldinozzi and K. E. Sickafus, *Phys. Rev. Lett.*, 2012, **108**, 195504.

6 C. Chaïrat, E. H. Oelkers, J. Schott and J. E. Lartigue, *J. Nucl. Mater.*, 2006, **354**, 14–27.

7 C. Z. Liao, K. Shih and W. E. Lee, *Inorg. Chem.*, 2015, **54**, 7353–7361.

8 K. Zhang, D. Yin, L. Peng and J. Wu, *Ceram. Int.*, 2017, **43**, 1415–1423.

9 K. Zhang, G. Wen, H. Zhang and Y. Teng, *J. Nucl. Mater.*, 2015, **465**, 1–5.

10 J. Chaumont, S. Soulet, J. C. Krupa and J. Carpena, *J. Nucl. Mater.*, 2002, **301**, 122–128.

11 Y. Huang, H. Zhang, X. Zhou and S. Peng, *J. Nucl. Mater.*, 2017, **485**, 105–112.

12 F. Gauthier-Lafaye, *Cryst. Phys.*, 2002, **3**, 839–849.

13 R. Bros, J. Carpena, V. Sere and A. Beltritti, *Radiochim. Acta*, 1996, **74**, 277–282.

14 E. R. Vance, C. J. Ball, B. D. Begg, M. L. Carter, R. A. Day and G. J. Thorogood, *J. Am. Ceram. Soc.*, 2003, **86**(7), 1223–1225.

15 E. R. Vance, Y. Zhang, T. McLeod and M. Jovanovic, *J. Nucl. Mater.*, 2012, **426**, 223–225.

16 J. Rakovan, R. J. Reeder, E. J. Elzinga, D. J. Cherniak, C. D. Tait and D. E. Morris, *Environ. Sci. Technol.*, 2002, **36**, 3114–3117.

17 R. Ravikumar, B. Gopal and H. Jena, *Inorg. Chem.*, 2018, **57**, 6511–6520.

18 B. P. Mandal and A. K. Tyagi, *J. Alloys Compd.*, 2007, **437**, 260–263.

19 T. J. White and D. ZhiLi, *Acta Crystallogr., Sect. B: Struct. Sci.*, 2003, **59**, 1–16.

20 P. V. Balachandran and K. Rajan, *Acta Crystallogr., Sect. B: Struct. Sci.*, 2012, **68**, 24–33.

21 M. L. Tate, D. A. Blom, M. Avdeev, H. E. A. Brand, G. J. McIntyre, T. Vogt and I. R. Evans, *Adv. Funct. Mater.*, 2017, **27**, 1605625.

22 S. S. Pramana, T. J. White, M. K. Schreyer, C. Ferraris, P. R. Slater, A. Orera, T. J. Bastow, S. Mangold, S. Doyle, T. Liu, A. Fajar, M. Srinivasan and T. Baikie, *Dalton Trans.*, 2009, **39**, 8280.

23 Y. N. Fang, C. Ritter and T. J. White, *Dalton Trans.*, 2014, **43**, 16031–16043.

24 E. N. Bulanov, J. Wang, A. V. Knyazev, T. White, M. E. Manyakina, T. Baikie, A. N. Lapshin and Z. Dong, *Inorg. Chem.*, 2015, **54**, 11356–11361.

25 C. Cao, S. Chong, L. Thirion, J. C. Mauro, J. S. McCloy and A. Goel, *J. Mater. Chem. A*, 2017, **5**, 14331–14342.

26 F. Lu, T. Yao, Y. Danon, J. Zhou, R. C. Ewing and J. Lian, *J. Am. Ceram. Soc.*, 2015, **98**, 3361–3366.

27 M. J. Rigali, P. V. Brady and R. C. Moore, *Am. Mineral.*, 2016, **101**, 2611–2619.

28 R. M. Asmussen, J. J. Neeway, A. R. Lawter, T. G. Levitskaia, W. W. Lukens and N. P. Qafoku, *J. Nucl. Mater.*, 2016, **480**, 393–402.

29 E. E. Jay, P. C. M. Fossati, M. J. D. Rushton and R. W. Grimes, Prediction and Characterisation of Radiation Damage in Fluorapatite, *J. Mater. Chem. A*, 2015, **3**, 1164–1173.

30 J. Sansom, *State Ionics*, 2004, **167**, 17–22.

31 A. Orera, E. Kendrick, D. C. Apperley, V. M. Orera and P. R. Slater, *Dalton Trans.*, 2008, **39**, 5296.

32 O. Terra, N. Dacheux, F. Audubert and R. Podor, *J. Nucl. Mater.*, 2006, **352**(1–3), 224–232.

33 B. H. Toby, *J. Appl. Crystallogr.*, 2001, **34**, 210–213.

34 A. N. Radhakrishnan, P. P. Rao, K. S. M. Linsa, M. Deepa and P. Koshy, *Dalton Trans.*, 2011, **40**, 3839.

35 M. Halvarsson, V. Langer and S. Vuorinen, *Surf. Coat. Technol.*, 1995, **76–77**, 358–362.

36 J. Ouyang, C. I. Ratcliffe, D. Kingston, B. Wilkinson, J. Kuijper, X. Wu, J. A. Ripmeester and K. Yu, *J. Phys. Chem. C*, 2008, **112**, 4908–4919.

37 T. An, A. Orera, T. Baikie, J. S. Herrin, R. O. Piltz, P. R. Slater, T. J. White and M. L. Sanjuán, *Inorg. Chem.*, 2014, **53**, 9416–9423.

38 S. Lambert, A. Vincent, E. Bruneton, S. Beaudet-Savignat, F. Guillet, B. Minot and F. Bouree, *J. Solid State Chem.*, 2006, **179**, 2602–2608.

39 J. P. Lafon, E. Champion and D. Bernache-Assollant, *J. Eur. Ceram. Soc.*, 2008, **28**, 139–147.

40 H. El Feki, J. M. Savariault and A. Ben Salah, *J. Alloys Compd.*, 1999, **287**, 114–120.

41 R. Wu, W. Pan, X. Ren, C. Wan, Z. Qu and A. Du, *Acta Mater.*, 2012, **60**, 5536–5544.

42 E. Rodríguez-Reyna, A. F. Fuentes, M. Maczka, J. Hanuza, K. Boulahya and U. Amador, *J. Solid State Chem.*, 2006, **179**, 522–531.

43 M. Wierzbicka-Wieczorek, M. Göckeritz, U. Kolitsch, C. Lenz and G. Giester, *Eur. J. Inorg. Chem.*, 2015, **2015**, 948–963.

44 A. F. Khan, M. Awais, A. S. Khan, S. Tabassum, A. A. Chaudhry and I. U. Rehman, *Appl. Spectrosc. Rev.*, 2013, **48**, 329–355.

45 A. Antonakos, E. Liarokapis and T. Leventouri, *Biomaterials*, 2007, **28**, 3043–3054.

46 J. Chen, Z. Yu, P. Zhu, J. Wang, Z. Gan, J. Wei, Y. Zhao and S. Wei, *J. Mater. Chem. B*, 2015, **3**, 34–38.

47 K. Boughzala, E. B. Salem, F. Kooli, P. Gravereau and K. Bouzouita, *J. Rare Earths*, 2008, **26**, 483–489.

48 R. E. Ouenzerfi, C. Goutaudiera, G. Panczer, B. Moine, M. T. Cohen-Adad, M. Trabelsi-Ayedi and N. Kbir-Ariguib, *Solid State Ionics*, 2003, **156**, 209–222.

49 R. Elouenzerfi, M. Cohenadad, C. Goutaudier and G. Panczer, *Solid State Ionics*, 2005, **176**, 225–231.

50 A. Awonusi, M. D. Morris and M. M. J. Tecklenburg, *Calcif. Tissue Int.*, 2007, **81**, 46–52.

51 A. R. Cassella, R. C. de Campos, S. Garrigues, M. de la Guardia and A. Rossi, *Fresenius' J. Anal. Chem.*, 2000, **367**, 556–561.

52 Y. Fang, S. J. Page, G. J. Rees, M. Avdeev, J. V. Hanna and T. J. White, *Inorg. Chem.*, 2018, **57**, 9122–9132.

53 N. Y. Mostafa, H. M. Hassan and O. H. Abd Elkader, *J. Am. Ceram. Soc.*, 2011, **94**, 1584–1590.

54 H. Njema, K. Boughzala, H. Boughzala and K. Bouzouita, *J. Rare Earths*, 2013, **31**, 897–904.

55 M. Palard, E. Champion and S. Foucaud, *J. Solid State Chem.*, 2008, **181**, 1950–1960.

56 C. S. Ciobanu, S. L. Iconaru, F. Massuyeau, L. V. Constantin, A. Costescu and D. Predoi, *J. Nanomater.*, 2012, **2012**, 1–9.

57 A. Jillavenkatesa and R. A. Condrate, *Spectrosc. Lett.*, 1998, **31**, 1619–1634.

58 V. Pecharsky and P. Zavalij, *Fundamentals of Powder Diffraction and Structural Characterization of Materials*, Springer Science & Business Media, 2008.

59 K. Momma and F. Izumi, *J. Appl. Crystallogr.*, 2011, **44**, 1272–1276.

60 Y. Luo, J. M. Hughes, J. Rakovan and Y. Pan, *Am. Mineral.*, 2009, **94**, 345–351.

61 G. Li, Y. Zhang, D. Geng, M. Shang, C. Peng, Z. Cheng and J. Lin, *ACS Appl. Mater. Interfaces*, 2012, **4**, 296–305.

62 J. M. Hucrrns and An. N. MlnuNo, *Am. Mineral.*, 1991, **76**, 1165–1173.

63 C. Meis, J. D. Gale, L. Boyer, J. Carpena and D. Gosset, *J. Phys. Chem. A*, 2000, **104**, 5380–5387.

64 A. Chartier, C. Meis and J. D. Gale, *Phys. Rev. B: Condens. Matter Mater. Phys.*, 2001, **64**, 085110.

65 C. Meis, *J. Nucl. Mater.*, 2001, **289**, 167–176.

66 G. Blasse, *J. Solid State Chem.*, 1975, **14**, 181–184.

67 J. A. Peterson, J. V. Crum, B. J. Riley, R. M. Asmussen and J. J. Neeway, *J. Nucl. Mater.*, 2018, **510**, 623–634.

68 J. G. Li, T. Ikegami and T. Mori, *Acta Mater.*, 2004, **52**, 2221–2228.

69 M. W. D. Cooper, C. R. Stanek and D. A. Andersson, *Acta Mater.*, 2018, **150**, 403–413.

70 R. S. Krishnan, R. Srinivasan and S. Devanarayanan, *Thermal expansion of crystals*, Elsevier, 1979.

71 R. Venkata Krishnan, G. Panneerselvam, M. P. Antony and K. Nagarajan, *J. Nucl. Mater.*, 2010, **403**, 25–31.

72 A. V. Knyazev, M. E. Komshina, A. V. Zhidkov and A. S. Plesovskikh, *Russ. J. Inorg. Chem.*, 2013, **58**, 1172–1176.

73 S. Yamazaki, T. Yamashita, T. Matsui and T. Nagasaki, *J. Nucl. Mater.*, 2001, **294**, 183–187.

74 A. V. Knyazev, E. N. Bulanov and V. Zh. Korokin, *Mater. Res. Bull.*, 2015, **61**, 47–53.

75 A. V. Knyazev, N. G. Chernorukov and E. N. Bulanov, *Mater. Chem. Phys.*, 2012, **132**, 773–781.

76 K. Fukuda, T. Asaka and T. Uchida, *J. Solid State Chem.*, 2012, **194**, 157–161.

77 L. G. Van Uitert, H. M. O'Bryan, M. E. Lines, H. J. Guggenheim and G. Zydzik, *Mater. Res. Bull.*, 1977, **12**, 261–268.

78 J. Feng, B. Xiao, R. Zhou and W. Pan, *Acta Mater.*, 2013, **61**, 7364–7383.

79 P. Zhang, Y. Zhao and X. Wang, *Dalton Trans.*, 2015, **44**, 10932–10938.

80 C. Wang, L. Guo, Y. Zhang, X. Zhao and F. Ye, *Ceram. Int.*, 2015, **41**, 10730–10735.

81 L. Glasser and H. D. B. Jenkins, *J. Am. Ceram. Soc.*, 2000, **122**, 632–638.

82 S. J. Patwe, B. R. Ambekar and A. K. Tyagi, *J. Alloys Compd.*, 2005, **389**, 243–246.

83 L. Guo, Y. Zhang, X. Zhao, C. Wang and F. Ye, *Ceram. Int.*, 2016, **42**, 583–588.